CrossMark

TECHNICAL PAPER

Thermo-mechanical analysis of the MIG/MAG multi-pass welding process on AISI 304L stainless steel plates

Rodrigo M. Farias[1] · Paulo R. F. Teixeira[1] · Douglas B. Araújo[1]

Abstract Welding processes on plates involve complex physical and chemical phenomena which make mathematical modeling difficult. Although coupled thermal-mechanical-metallurgical effects are important, good results can usually be found when numerical models based on heat transfer equation and governing equations of the structural behavior are used. In this paper, a numerical analysis of multi-pass single V-groove weld in butt joint (three passes) of AISI 304L stainless steel, using the conventional MIG/MAG process is presented. The plates are 9.6 mm thick, 200 mm long and 50 mm wide. The numerical simulations were performed by ANSYS® Multiphysics software, considering a moving heat source with Gaussian type distribution, convection and radiation heat transfer on the surfaces and temperature-dependent material properties, for both mechanical and thermal simulations. The von Mises yield criterion and associated flow rule are used together with kinematic hardening and a bilinear representation of the stress–strain curve. The element birth and death technique is employed to consider an appropriate analysis of the welding processes with material deposition. The fusion zone shape, thermal cycles and final distortion of the plates obtained from the experiments developed in the laboratory of research in welding engineering (LAPES–FURG), located in Rio Grande, RS, Brazil, are compared with numerical results. In general, both thermal and mechanical results obtained by numerical simulation are in good agreement with experimental ones. Analysis of the influence of each pass on the plate distortion is discussed.

Keywords Welding process · Numerical simulation · Heat source model · Element birth and death

1 Introduction

The application of the numerical simulation to the welding process has recently grown mainly due to the increase in the capacity of computers and the availability of commercial numerical codes. However, many assumptions and approximations are still necessary due to the complexity of phenomena involved in this process. The first studies of numerical simulation of welding process were carried out by Friedman [1] who developed a thermal-mechanical model based on the finite element method (FEM) to calculate temperature, stress and distortion distributions. Lindgren [2] and Dong [3] have shown that thermal-mechanical decoupled analysis provides accurate results and simplifies the numerical solution. Similarly, other authors, such as Brickstad and Josefson [4], Capriccioli and Frosi [5], Coret and Combescure [6], Wu et al. [7] and El-Ahmar [8] have stated that the influence of the mechanical model on thermal and metallurgical simulations is not significant in the welding process application. However, coupling between thermal and metallurgical analyses is employed to determine temperature and phase fraction fields.

The main difficulty of the thermal field simulation in a welding process is the heat source modeling. After
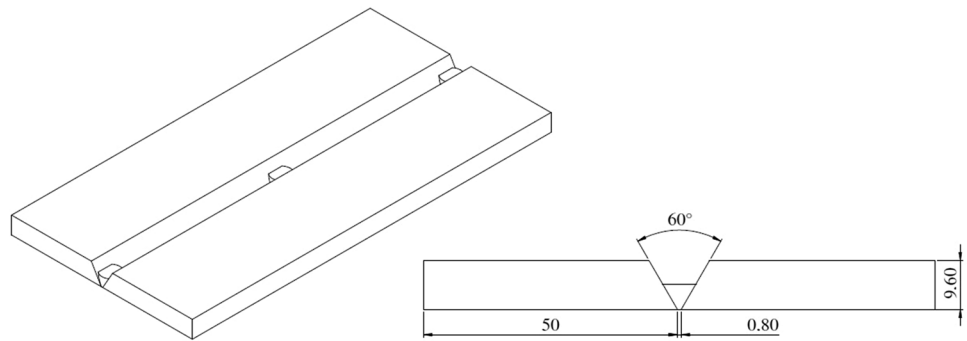
✉ Paulo R. F. Teixeira
pauloteixeira@furg.br

Rodrigo M. Farias
rodrigofarias.mec@gmail.com

Douglas B. Araújo
douglasbafurg@gmail.com

[1] Universidade Federal do Rio Grande, FURG, Campus Carreiros, Av. Itália km 8, Rio Grande, Rio Grande do Sul, Brazil

Fig. 1 Sketch of the specimen (dimensions in mm)

Rosenthal [9] proposed the analytical solution considering a punctual or a line heat source, several more realistic heat source distributions have been developed. Pavelic et al. [10] developed a surface heat source model with a Gaussian distribution. After that, Eagar and Tsai [11], Cho and Kim [12], Deng et al. [13] and Rayamyaki et al. [14] also studied and applied the same heat source model. Other researchers, such as Balasubramanian et al. [15], Zaeh and Schober [16] and Ziolkowski and Brauer [17], proposed the combination of Gaussian distribution on the surface and the distribution along the thickness to consider a 3D model, by applying the conical Gaussian heat source one. A classical volumetric heat source model is the double ellipsoid distribution that was developed by Goldak et al. [18]. Wahab et al. [19] and Wu et al. [7] combined the double ellipsoid with spherical and cylindrical volumes, respectively, along the thickness.

The application of a methodology to the numerical thermal-mechanical analysis to represent the fusion zone during the welding process is another difficulty which increases in multi-pass cases. During the material deposition, numerical models must consider elements of weld beads stress-free while the temperature is higher than the solidification one. Moreover, accumulated plastic strains and stresses must be relaxed in existing materials when they are subject to annealing effects. The nodal birth method [20], the strain relaxation method [21] and the element birth and death method [22, 23] are the main techniques to model this phenomenon.

In this paper, a welding numerical analysis of multi-pass single V-groove weld in butt joint of AISI 304L stainless steel is carried out by the conventional MIG/MAG process. The numerical simulations were performed by ANSYS® Multiphysics software, considering a moving heat source with Gaussian type distribution, convection and radiation heat transfer on the surfaces and temperature-dependent material properties for both mechanical and thermal simulations. The von Mises yield criterion and associated flow rule is used together with kinematic hardening and a bilinear representation of the stress–strain curve. The element birth and death method is employed to consider the weld filler deposition along the welding process. Data on the fusion zone shape, thermal cycles and final distortion of the plates, obtained from the experiments developed at the laboratory of research in welding engineering (LAPES) at the Universidade Federal do Rio Grande (FURG), are compared with numerical ones.

2 Case study

The case study is a welding process of multi-pass butt welds (root pass and two filling passes) which was studied numerically and experimentally. The experiments were carried out at the LAPES–FURG. The material of the plates is the AISI 304L stainless steel and the welding process is the conventional MIG/MAG with Argon and 2 % O_2 in a flow rate of 2.67×10^{-4} m³/s (16 l/min). The plates, which are 9.6 mm thick, 200 mm long, 50 mm wide, are initially positioned by three tack welds; the chamfer is a 60 degree V-type (Fig. 1). Welding with weaving was used for the second filling pass in which the weave frequency was 3 Hz and the weave amplitude was 6 mm. Welding were conducted by using the 6-axis weld robot Motoman HP20D (repeatability = ±0.06 mm) and the Power Wave® 455 M/STT Advanced Process Welder. Three experiments were carried out with the objective of assessing the repeatability of the results.

Temperatures at four points were measured by thermocouples (type K) located at the opposite face of the weld, whose distances from the weld center line are 4, 8, 12, and 16 mm at the bottom and middle of the plates in longitudinal direction. They were attached to the metal plate with the use of a capacitive discharge. The data acquisition measurement system was the NI9211 model of National Instruments (accuracy <0.07 K) with 3.5 sample/s/ch and resolution of 24 bits. Plate deformations were measured by the coordinate measuring machine Hexagon Metrology—Global Classic (resolution of 1 μm).

Parameters of voltage, current, welding speed and distance from the electrode to the plate surface (DE) of the welding process are shown in Table 1 for each pass.

Table 1 Parameters of welding process

Parameters	Root pass	First filling pass	Second filling pass
Voltage U (V)	16.7	23.0	23.0
Current I (A)	161	226	226
Welding speed v (mm/s)	4.16	4.83	4.83
DE (mm)	12	18	18

DE distance from the contact tip to the plate surface

3 Theoretical concepts

3.1 Thermal analysis

The thermal field is governed by the heat conduction equation given by

$$\frac{\partial}{\partial x}\left(k(T)\frac{\partial T}{\partial x}\right) + \frac{\partial}{\partial y}\left(k(T)\frac{\partial T}{\partial y}\right)$$
$$+ \frac{\partial}{\partial z}\left(k(T)\frac{\partial T}{\partial z}\right) + Q_V = \rho(T)C_p(T)\frac{\partial T}{\partial t} \quad (1)$$

where, T is the temperature, $k(T)$ is the thermal conductivity, $\rho(T)$ is the specific mass, $C_p(T)$ is the specific heat and Q_V is the rate at which energy is generated per unit volume of the medium (in this study, Q_V is null).

A phase change with melting and solidification is involved in the welding process. Enthalpy methods are some of several techniques to deal with this type of problem [24]. The essential feature of basic enthalpy methods is that the evolution of the latent heat is accounted for the enthalpy as well as the relation between enthalpy and temperature. These methods are based on the heat conduction equation expressed in the function of the enthalpy (H) as follows:

$$\frac{\partial}{\partial x}\left(k(T)\frac{\partial T}{\partial x}\right) + \frac{\partial}{\partial y}\left(k(T)\frac{\partial T}{\partial y}\right)$$
$$+ \frac{\partial}{\partial z}\left(k(T)\frac{\partial T}{\partial z}\right) = \frac{\partial[H(T)]}{\partial t} \quad (2)$$

where, Q_V is intentionally omitted and enthalpy H is the integral of the heat capacity with respect to temperature:

$$H = \int \rho(T)\,C_p(T)\,\mathrm{d}T \quad (3)$$

In Eqs. (2) and (3), the latent heat must be considered for the phase change region. The numerical method used in this study is shown in Sect. 4.

The thermodynamic boundary conditions on the external surfaces of the solid comprise heat transfer for convection and radiation. The heat flow density for convection (q_c) in the environment gas or liquid is given by Newton's heat transfer law:

$$q_c = h_c(T - T_0) \quad (4)$$

where, T is the temperature of the external surface, T_0 is the temperature of gas or liquid and h_c is the coefficient of convective heat transfer. This coefficient depends on the convection conditions on the solid surface, besides the properties of the surface and the environment. Some authors, such as Sorensen [25], Teng et al. [26], Gery et al. [27] and Smith and Smith [28], have proposed values of coefficient of convective heat transfer from 5 to 20 W/m² K.

The heat flow density for radiation q_r is governed by the Stefan–Boltzmann law, as follows

$$q_r = \varepsilon_r \sigma_r (T^4 - T_0^4) \quad (5)$$

where, ε_r is the emissivity of the material surface and σ_r is the Stefan–Boltzman constant. The value of the emissivity depends on the temperature in the welding process ([29, 30]), in which it ranges from room temperature to approximately 1450 °C. In general, the higher the temperature, the larger the emissivity.

In this study, the heat of the welding arc was modeled by a traveling two-dimensional distribution of a heat source with a Gaussian distribution. Therefore, the heat flux distribution on the surface of the solid is related to the radial position r (whose origin is the arc center), given by [31]

$$q(r) = \frac{\eta U I}{2\pi\sigma^2} e^{-(r^2/2\sigma^2)} \quad (6)$$

where, $q(r)$ is the surface flux at radius r, η is the efficiency coefficient, U is the voltage, I is the current and σ is the radial distance from the center. The surface flux is reduced by 5 % when the $r = 2.45\sigma$ and it is practically null when $r = 3\sigma$ [31].

3.2 Mechanical analysis

In the mechanical analysis, the temperature history obtained by the thermal analysis is the thermal loading input in the structural model. The total strain rate is decomposed into three components, as follows:

$$\varepsilon = \varepsilon^e + \varepsilon^p + \varepsilon^{th} \quad (7)$$

where, ε^e, ε^p, and ε^{th} are elastic, plastic and thermal strain rates, respectively. The elastic strain is modeled using the
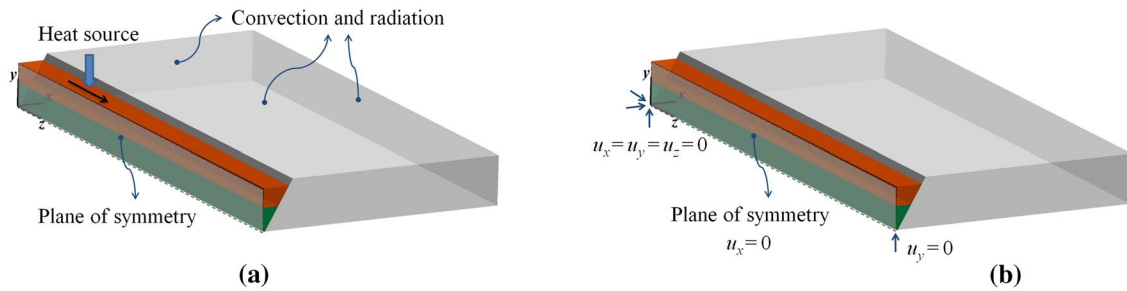
Fig. 2 Sketches of the computational domains in thermal (**a**) and mechanical (**b**) analyses
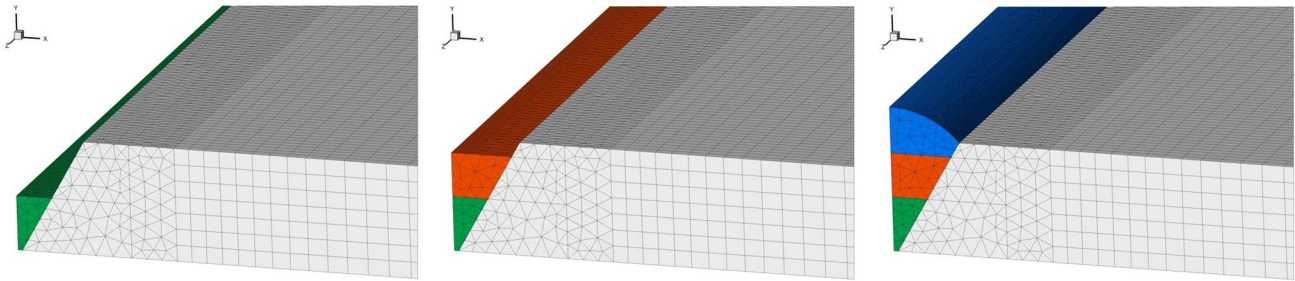

Fig. 3 Meshes for computational domain with only root pass, both root and first filling passes and all passes

isotropic Hooke's law with temperature-dependent Young's modulus and Poisson's ratio. Regarding the plastic strain, a plastic model is employed with a yield surface by considering temperature dependent mechanical properties. The thermal strain is calculated by using temperature-dependent coefficient of thermal expansion.

4 Thermo-mechanical numerical model

The numerical analysis consists of a transient thermal evaluation to determine temperature distributions at each time step for all passes and subsequent mechanical analysis using the temperature fields as thermal conditions. The software used in this study is ANSYS® Multiphysics 15.0 which solves the transient thermal and mechanical equations using the FEM. Hexahedral elements with eight nodes are employed in both thermal (SOLID70) and mechanical analyses (SOLID185) whereas surface elements (SURF152) are used for imposing the radiation condition in the thermal evaluation. In the mechanical analysis, the thermal hexahedral elements are changed to mechanical ones and, in this case, surface elements are deactivated using the element birth and death technique. This technique is also adopted to simulate the welding filler deposition along time. This method deactivates elements by multiplying their stiffness by a severe reduction factor. Although zeroed out of the load vector, element loads associated with deactivated still appear in element-load lists.

Figure 2 shows a stretch of the computational domain used by thermal and mechanical analyses and an indication of the imposed boundary conditions. Half of the domain is used by the simulations, due to the symmetrical behavior in relation to the plane that passes by the welding center line. Axis x and z of the Cartesian coordinate system of the computational domain are on the plane of the plates; axis x is in transversal direction and axis z is in longitudinal one (direction of the heat source movement).

Figure 3 shows three meshes with (a) only root pass, (b) both root and first filling passes and (c) all passes. The mesh refinement occurs in the welding region where temperature, distortion and stress gradients are higher. A mesh convergence study was carried out in the thermal analysis by comparing time series of temperatures obtained numerically for the three passes at four points located at the same position of the thermocouples. In this study, subsequent meshes with sizes of the element sides of 1.2, 1.0, and 0.9 mm are analysed. Low differences of the peak temperatures between consecutive meshes were found (lower than 2 °C in all cases). Due to the computational cost, the intermediate mesh (1.0 mm) that had 106376 elements and 40,044 nodes, was chosen to the simulation.

4.1 Thermal numerical model

In the thermal numerical model, the heat flux is imposed at each time step Δt on nodes that belong to the external surface covered by the region defined by the Gaussian source

function (Eq. 4). The updated position of the center of the Gaussian heat source (z_0) is calculated according to the welding speed ($z_0 = v\,t$). Therefore, the radial position (r), as the heat source advances, is given by

$$r = \sqrt{x^2 + (z - z_0)^2} \tag{8}$$

The spatial advance of the center of the heat source at each time step (Δt) is equal to the size of the element on the weld center line. Therefore, the time step (Δt) is calculated according to the welding speed of each pass shown in Table 1, resulting in 0.239 s for the root pass and 0.206 s for the filling passes. The simulation lasted 44 s for the root pass and 31 s for both first and second filling passes.

In all nodes of the computational domain, temperature of 20 °C is imposed as the initial condition for the root pass. The maximum temperature between passes (after the cooling process) is 50 °C for both numerical simulation and experiment. The convection and radiation dissipations to the environment are considered on all external surfaces of the domain as a boundary condition, except the surfaces that belong to the plane of symmetry in which the normal heat flux is null (Fig. 2a).

In the application of the element birth and death technique to thermal analysis, deactivated elements have their enthalpy and other effects set to zero. Elements are activated as the heat source advances at each time step (Δt), according to the region defined by a circle whose ray is lower than 3σ.

The Newton–Raphson method is used in the transient thermal solution and, basically, the following steps are used in the thermal analysis:

(a) Deactivate all elements that belong to the filler material.
(b) For each time step (Δt) on the root pass:

    (b1) Calculate the updated position of the center of the Gaussian source (z_0).
    (b2) Activate the elements and select nodes that belong to the filling material in the region defined by the Gaussian source function.
    (b3) Impose the heat flux to the select nodes according to the Gaussian source function.
    (b4) Solve the heat conduction problem.

(c) Solve the problem during cooling.
(d) Repeat steps (b) and (c) for the other passes.

The precise calculation of the filled volume related to each pass by using the mass conservation was based on feed velocity, wire diameter and welded length obtained by
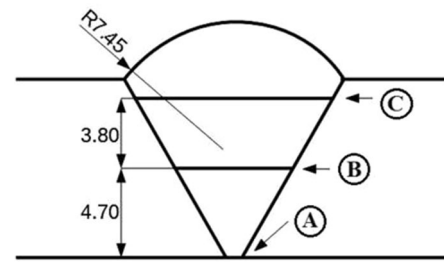

Fig. 4 Depth of each pass in computational domain (dimensions in mm)

experimental data. Therefore, the depth of each pass was determined as shown in Fig. 4.

Thermal properties of the stainless steel AISI 304L used in numerical simulations are temperature dependent. To deal with this type of phase change problem, ANSYS® Multiphysics employs the enthalpy method described by Tamma and Raju [32]. In this method, the latent heat during the phase change is taken into consideration by varying the enthalpy abruptly. In this study, this variation occurs between the solidus temperature of 1350 °C and the liquidus temperature of 1400 °C and the latent heat is 260 J/g. Figure 5 shows the relation between thermal conductivity (k), specific mass and enthalpy (H) with temperature.

An equivalent thermal conductivity higher than the one at room temperature is used above the fusion temperature to consider the convection of melted material as suggested by Deng and Murakawa [33] and other authors. Emissivity is also temperature dependent and increases with the temperature in a range from 0.7 to 0.9, according to Touloukian and De Witt [34]. The coefficient of convective heat transfer is $h_c = 10$ W/m² °C.

4.2 Mechanical numerical model

In the mechanical model, the incremental calculation technique is employed for the thermal elastic–plastic analysis. In the application of the element birth and death technique to mechanical analysis, deactivated elements have their strains set null. When elements are reactivated, their stiffness, mass and element loads return to their full original values. Thermal strains are computed for newly activated elements according to the current load step temperature. In this study, only elements belonging to nodes with temperatures above 1300 °C are activated.

The mechanical numerical scheme is very similar to the thermal one and consists of the following steps:

(a) Deactivate all elements that belong to the filler material.
(b) For each time step (Δt) on the root pass:

1250

J Braz. Soc. Mech. Sci. Eng. (2017) 39:1245–1258

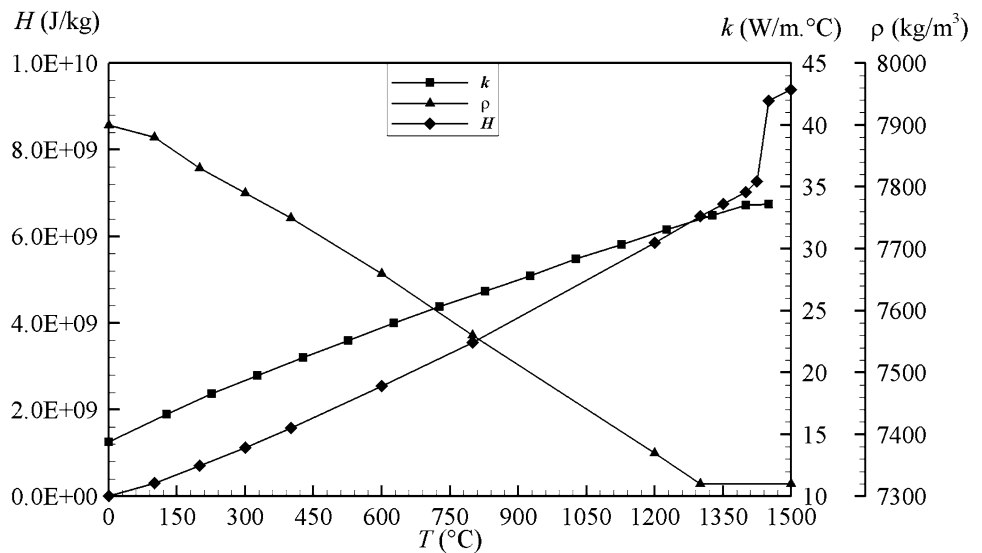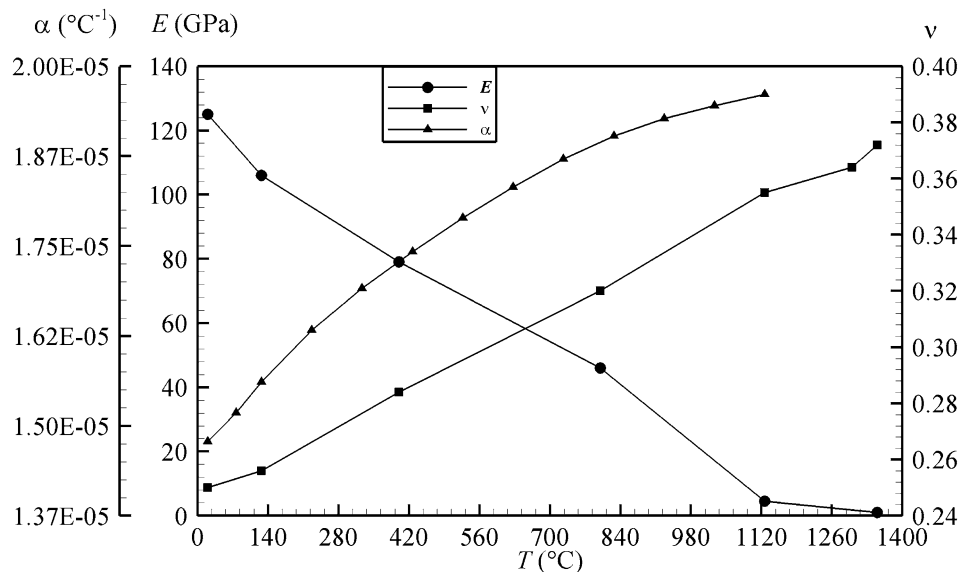**Fig. 5** Thermal properties of stainless steel AISI 304L

Fig. 6 Mechanical properties of stainless steel AISI 304L

(b1) Impose the node temperatures obtained in the thermal analysis at the same time step.

(b2) Activate elements and select nodes that belong to the filling material in the region according to the mechanical criterion.

(b3) Solve the mechanical equations.

(c) Solve equations during cooling.

(d) Repeat steps (b) and (c) for other passes material and geometric non-linearities are adopted by the mechanical analysis. A static solution at each time step whose initial condition is the final one obtained at previous time step is considered. Null values of displacements, deformations and stresses are taken into account at

the beginning of the welding process. The boundary condition is imposed to the displacements only to prevent the rigid body movement from interfering in plate deformations (Fig. 2b).

Mechanical properties of stainless steel AISI 304L are also temperature dependent. The Young's modulus (E), Poisson's ratio (ν) and thermal expansion coefficient related to the temperature are shown in Fig. 6. The elasto-plastic behavior, whose plastic model is bilinear kinematic hardening, is represented by temperature dependent curves of strain vs. stress in Fig. 7. Similar behavior was adopted by other authors, such as Brickstad and Josefson [4], Hong et al. [21] and Ohms et al. [35].
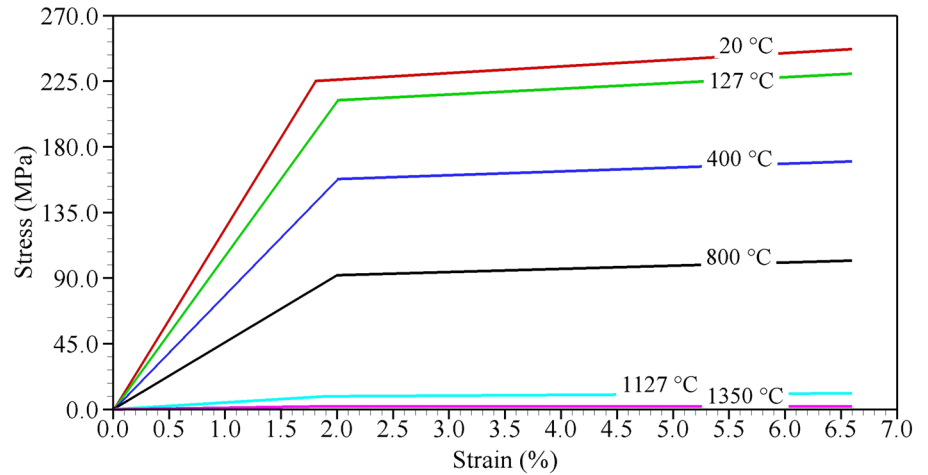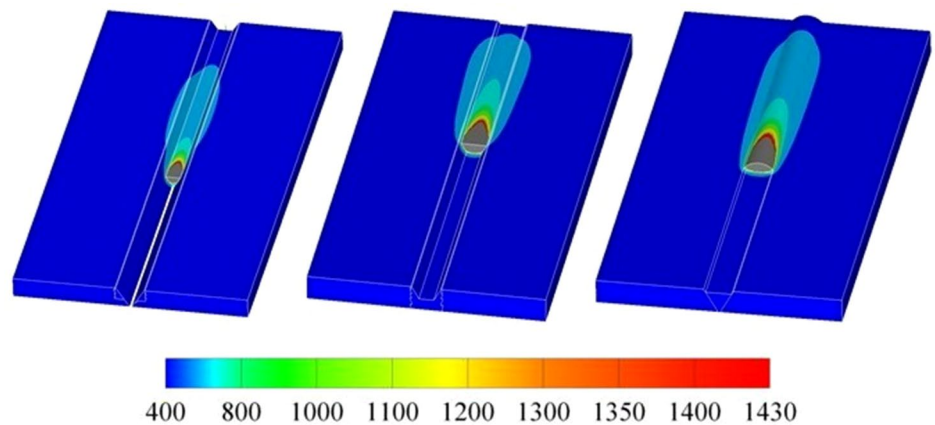
Fig. 7 Stress vs. strain for stainless steel AISI 304L

Fig. 8 Temperature distribution (°C) during the welding process

5 Results

5.1 Thermal results

Figure 8 shows the temperature distribution for the three passes at 22 s (root pass) and 15 s (first and second filling passes). Although figures show the whole computational domain, every simulation was carried out in half by using the symmetry condition. A high temperature gradient concentrated near the heat source is observed. Besides, the employment of the element birth and death technique enabled the filling material to be modeled according to the movement of the heat source.

An adequate validation of the thermal model in a welding process consists in comparing both thermal cycles and fusion zone shape obtained by simulations and experimental ones [28]. Therefore, the nodal temperatures are compared with those obtained by thermocouples from TC1 to TC4 (Fig. 9), whose distances from the weld center line are 4, 8, 12, and 16 mm, respectively, at the bottom and middle of the plates in longitudinal direction. The fusion zone
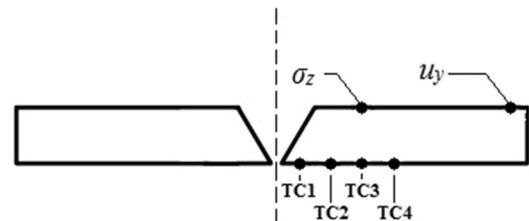

Fig. 9 Location of points used for comparisons of results

of the transversal section at the middle of the plates (at the same section of thermocouple positions), obtained by macrography, is also compared with that of numerical simulation. In this validation process, the efficiency (η) and the radial distance from the center (σ) in the heat source function are set to reach the best temperature curve adjustment in relation to the experimental ones. Therefore, η for all passes is 85 % and σ is 1.3 mm for the root pass, 2.0 mm for the first and 2.3 mm for the second filling passes. It is worth mentioning that the value of the efficiency found in
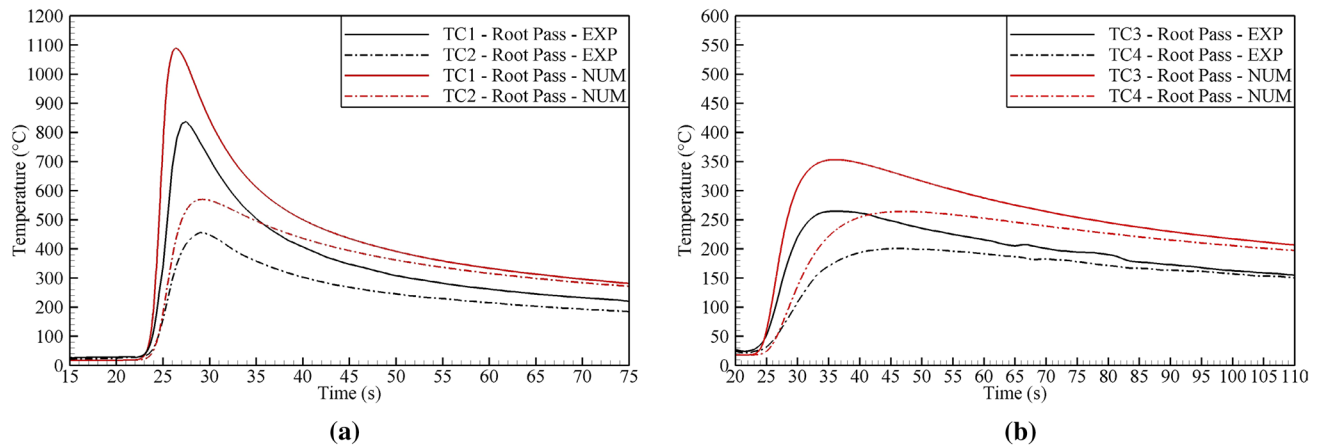
1252

J Braz. Soc. Mech. Sci. Eng. (2017) 39:1245–1258

Fig. 10 Thermal cycles at distances of **a** 4 and 8 mm (TC1 and TC2) and **b** 12 and 16 mm (TC3 and TC4) for the root pass
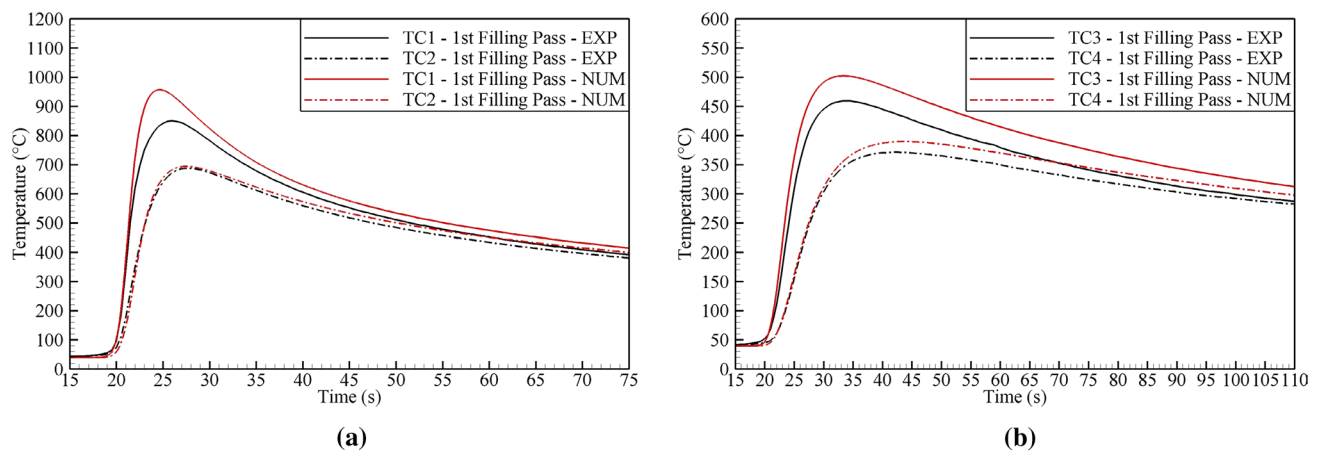

Fig. 11 Thermal cycles at distances of **a** 4 and 8 mm (TC1 and TC2) and **b** 12 and 16 mm (TC3 and TC4) for the first filling pass

this validation process is in the usual range for the MIG/MAG process [36].

Figure 10 shows the thermal cycles at the four positions (4 mm: TC1, 8 mm: TC2, 12 mm: TC3, and 16 mm: TC4) for the root pass. In general, the simulation of the root pass is more difficult, once there is a high heat flux concentrated in the lowest part of the chamfer, a fact that causes high thermal gradients in this zone and large differences between temperatures obtained by simulations and experiments. The slope of the temperature curve after the temperature peak represents the cooling rate, which is related to the heat transfer of the plate to the environment. In this case, the numerically obtained cooling rates are in good agreement with the experimental results. This fact leads to the conclusion that the boundary conditions, the coefficient of convective heat transfer and radiation conditions are well represented by the simulations.

Figure 11 shows the thermal cycles at the four positions (TC1, TC2, TC3, and TC4) for the first filling pass. The

peak temperature differences between numerical and experimental results are 12.5, 0.9, 9.3, and 4.8 % for 4, 8, 12, and 16 mm positions, respectively. In general, numerical results are in very good agreement with experimental ones. This fact is expected because, in this case, a less intensive thermal gradient occurs in comparison with the root pass, once the heat source is farther from the thermocouple positions. The position with the highest difference is 4 mm due to its proximity to weld bead. As in the root pass, the cooling rates are similar to the experimental ones.

Figure 12 shows thermal cycles at the four positions (TC1, TC2, TC3, and TC4) for the second filling pass. The peak temperature differences between numerical and experimental results are 5.7, 3.9, 1.9 e, 3.1 % for 4, 8, 12, and 16 mm positions, respectively. In all cases, there are excellent agreements between numerical and experimental results. As in the first filling pass, the thermal cycle of 4 mm has the highest difference by comparison with others due to its distance from the weld bead. It is worth
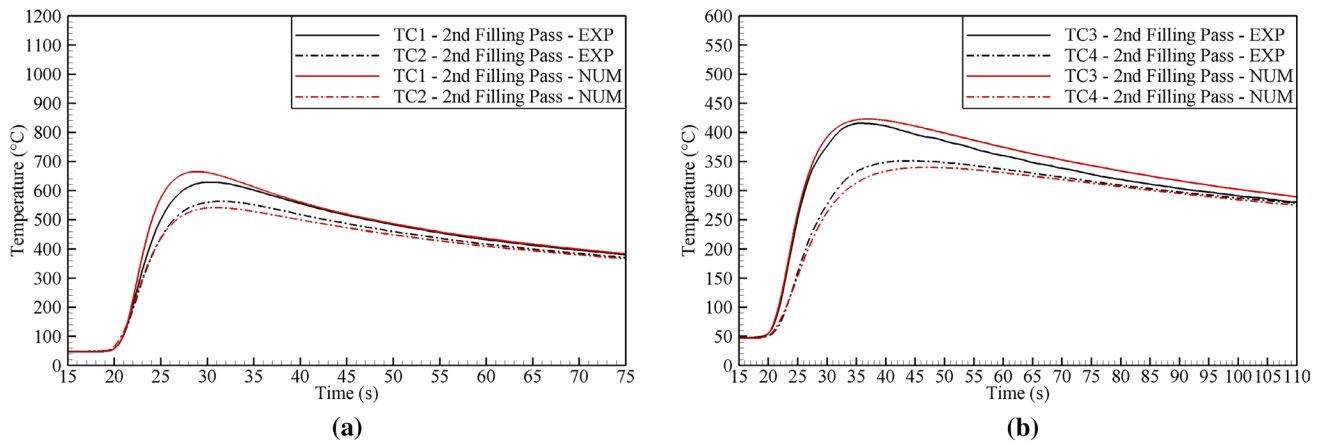
Fig. 12 Thermal cycles at distances of **a** 4 and 8 mm (TC1 and TC2) and **b** 12 and 16 mm (TC3 and TC4) for the second filling pass

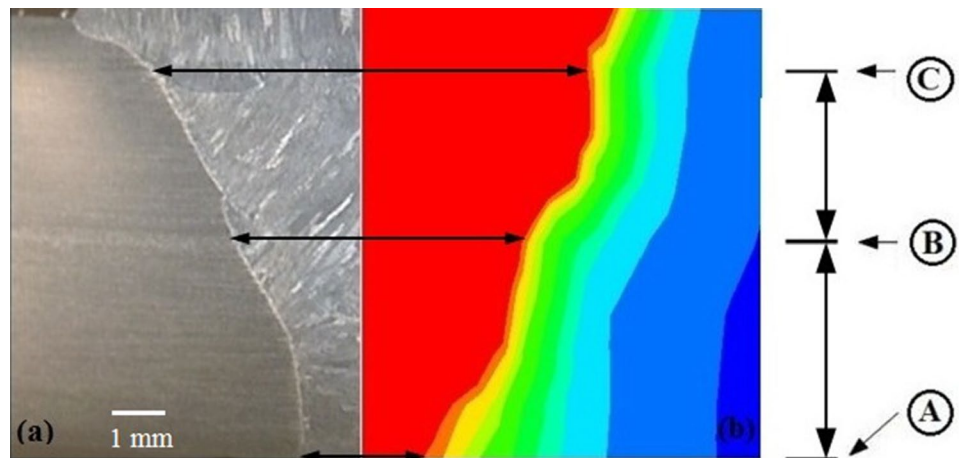**Fig. 13** Fusion zone shape **a** experimentally and **b** numerically obtained

Table 2 Widths of fusion zone shape at the root (A), the interface between the root and the first filling passes (B) and the interface between the first and the second filling passes (C)

Cases	A	B	C
Experimental (mm)	3.0	6.2	10.0
Numerical (mm)	2.6	6.9	9.8
Numerical vs. experimental (%)	12.0	12.2	2.0

zone at three levels of depth: the root (A), the interface between the root and the first filling passes (B) and the interface between the first and the second filling passes (C) (see Fig. 2). In general, numerical results are in good agreement with experimental ones. The largest difference occurs at the top of the plate, possibly because of the weaving process that is not reproduced in numerical simulations.

5.2 Mechanical results

Figure 14 shows distorted shape and displacement distribution of the plates after three-pass welding and the cooling step experimentally and numerically obtained. The angular distortions in the transversal section in the middle of the plate are shown in Fig. 15. Experimental and numerical results are in good agreement. The experiments show a final angular distortion of 3.7°, while the one of the numerical simulation is 3.1°. This figure also shows the angular distortion at the end of each pass after cooling obtained
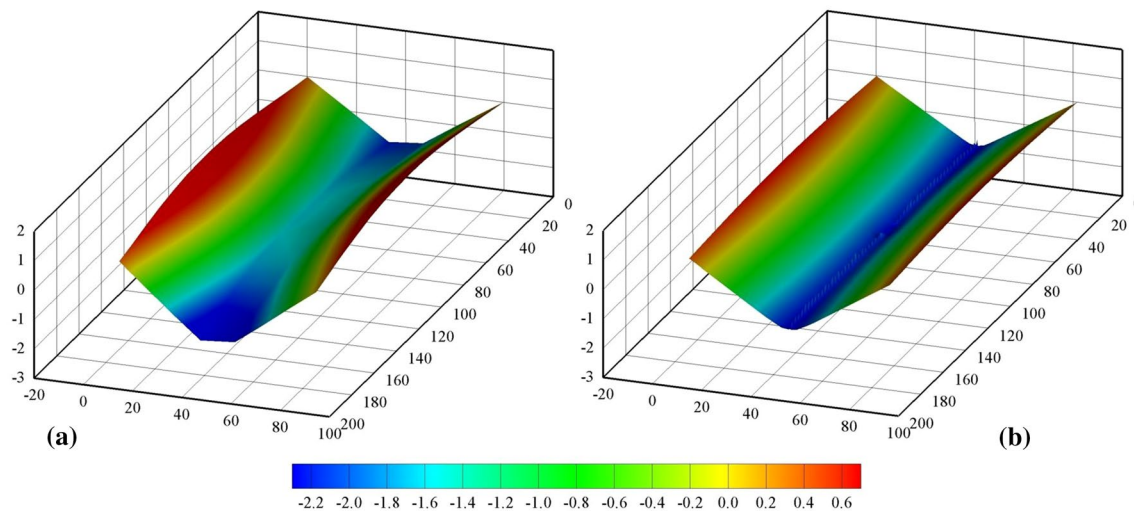
emphasizing that, even if the weaving was not considered, the results in terms of thermal cycles are very good, possibly because the longest distance among the heat source and the thermocouple positions for this pass. However, this effect appears in the fusion zone shape as described below. The cooling rates of all cases are very well simulated.

Figure 13 shows fusion zone shapes obtained numerically and experimentally: the red region indicates temperatures above 1430 °C (defined by boundary isotherm of 1430 °C). Table 2 presents widths of the fusion

1254

J Braz. Soc. Mech. Sci. Eng. (2017) 39:1245–1258

Fig. 14 Distorted shape and displacement distribution of the plates after three-pass welding and the cooling step: **a** experimental and **b** numerical results (dimensions in mm)

Fig. 15 Angular distortions, in the transversal section in the middle of the plate, numerically obtained at the end of each pass after cooling and experimentally obtained at the end of the welding (dimensions in mm)
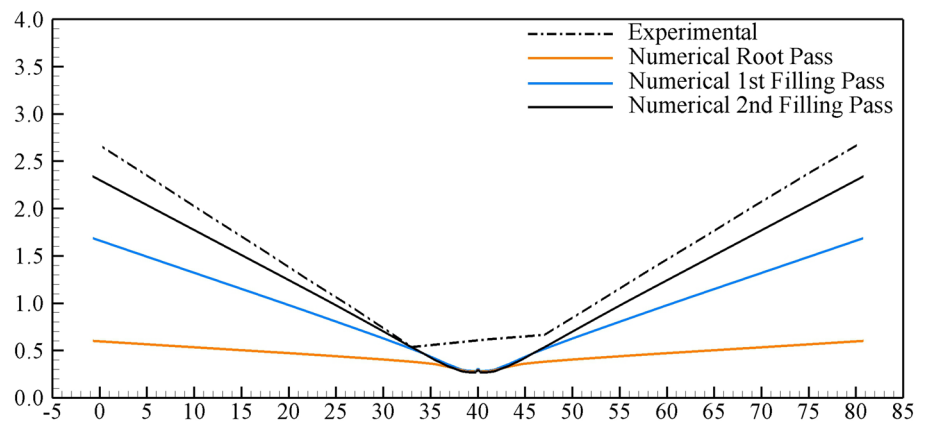
numerically. It is worth pointing out that the first filling pass gives larger contribution to the total angular distortion.

Figure 16 shows temporal series of three variables: (a) vertical displacement component at 45 mm from the welding center line in the middle of the plates u_y (see Fig. 8), (b) temperature T at the same position of TC3 (12 mm from the welding center line) and (c) longitudinal stress at the same distance from the thermocouple (TC3) position, but on the top of the plate σ_z. The monitoring position chosen for displacement is the one in which it is higher and influenced mainly by variations of stresses in regions near the weld bead. This is the reason why the monitoring point chosen for temperature and stress is located close to the weld bead.

The variation of displacement is larger during the welding process by comparison with that along the cooling, in which displacement increases smoothly. The increase of displacement during the welding process is noticed for root and first filling passes, whereas there is an initial decrease in the second

filling pass, before the increase at the end. Figure 16 shows that the largest displacement occurs at the end of first filling pass (0.64 mm at the end of root pass, 2.00 mm at the end of first filling pass and 2.58 mm at the end of the second filling pass).

Longitudinal stress σ_z experiments a fast compressive increase until the heat source passes its monitoring position and a tensile increase occurs sequentially. In the cooling process, the tensile continues smoothly until it almost reaches the yield stress.

Figure 17 shows longitudinal residual stress components on the top of the plate surface at the end of each passes after the cooling. Similar behaviors of stresses on the bottom surface are found. The region around the weld bead has higher tensile stresses which are approximately the yield stress near the weld bead, as expected. Far from the weld bead, longitudinal stresses become compressive. On the weld bead, the longitudinal stress has the same uniform behavior, with some variations near the plate edge.

J. Braz. Soc. Mech. Sci. Eng. (2017) 39:1245–1258

1255

Fig. 16 Temporal series of displacement component normal to the plane of plates at 45 mm from the welding *center line* in the *middle* of the plates (*u*); temperature *T* at the same position of TC3; and longitudinal stress σ_z at the same distance from the temperature position but on the *top* of the plate
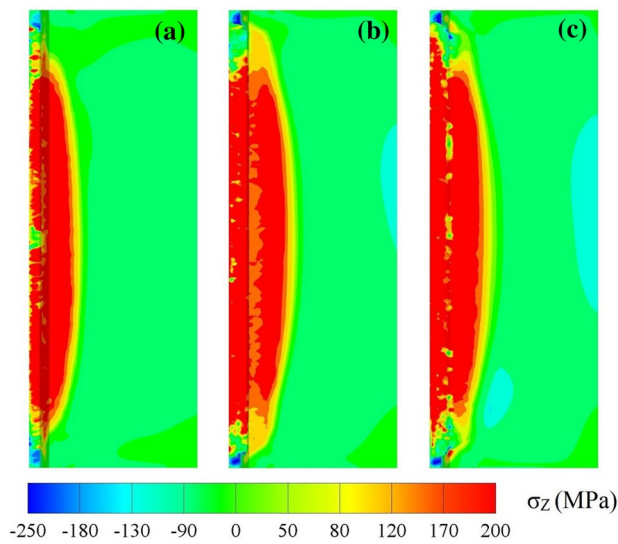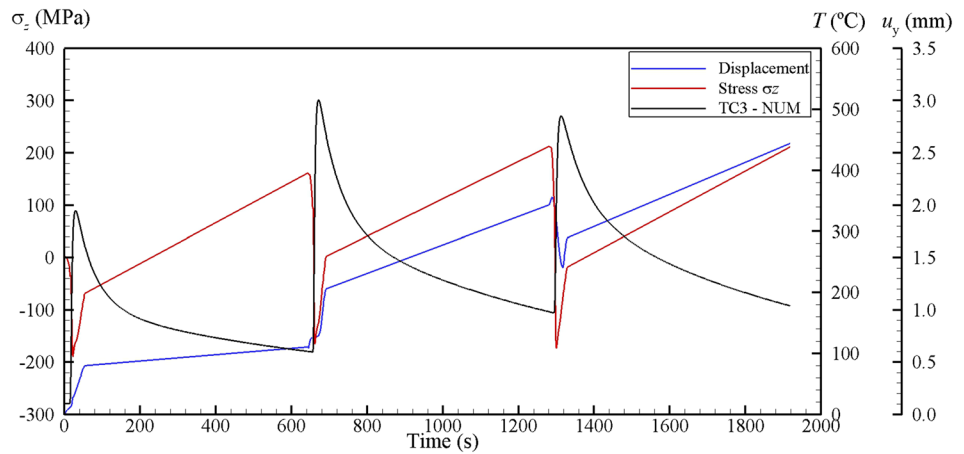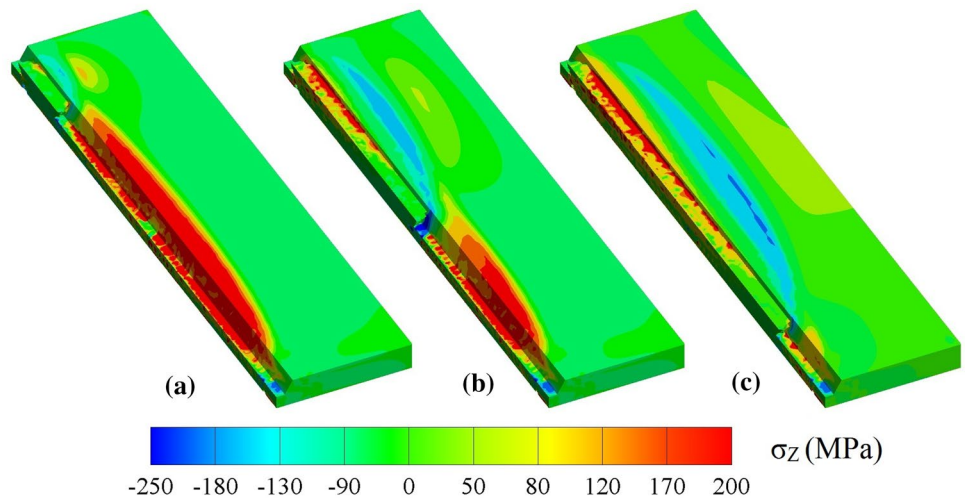

Fig. 17 Longitudinal residual stress components on the top of the plate at the end of **a** root, **b** first filling, and **c** second filling passes after cooling

Fig. 18 Longitudinal residual stress components in three instants along the first filling pass

The sequence of longitudinal stress components in three instants along the first filling pass is shown in Fig. 18. It can be noticed that the birth of elements occurs as the temperature reaches the fusion one along the structural simulation. This sequence shows that there is tensile stress in the region around the weld bead where the elements are not activated. It is the result of the residual stresses generated during the root pass and subsequent cooling. However, compressive stress occurs in the region farther from the weld bead as elements are born.

Figure 19 shows transverse residual stress components on the top of the plate surface at the end of each pass after cooling. The region around the weld bead has higher tensile stress, but they are lower than longitudinal ones. Near the plate edges, transverse stress components are compressive.

Figures 20 and 21 show longitudinal and transverse stresses on the top of the plate along a line 12 mm from the weld bead and parallel to it for each pass. The longitudinal stresses for the three passes have similar behavior and the magnitude is almost constant and close to the yield stress of material far from the plate edges. The magnitude
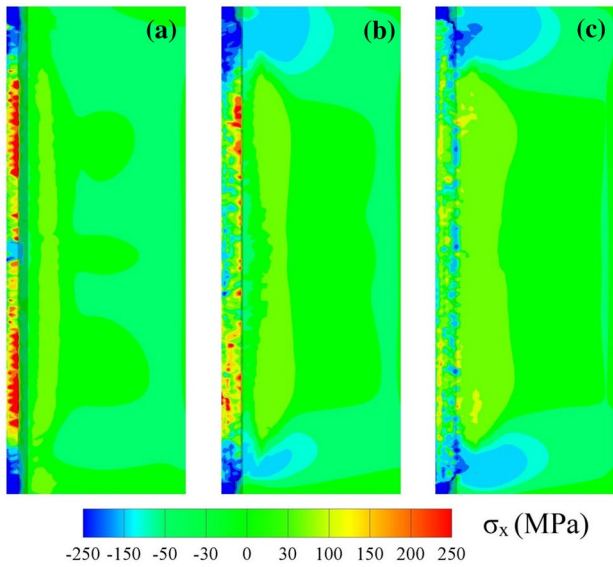
σ_x (MPa)

-250 -150 -50 -30 0 30 100 150 200 250

Fig. 19 Transverse residual stress components on the top of the plate at the end of **a** root, **b** first filling, and **c** second filling passes after cooling
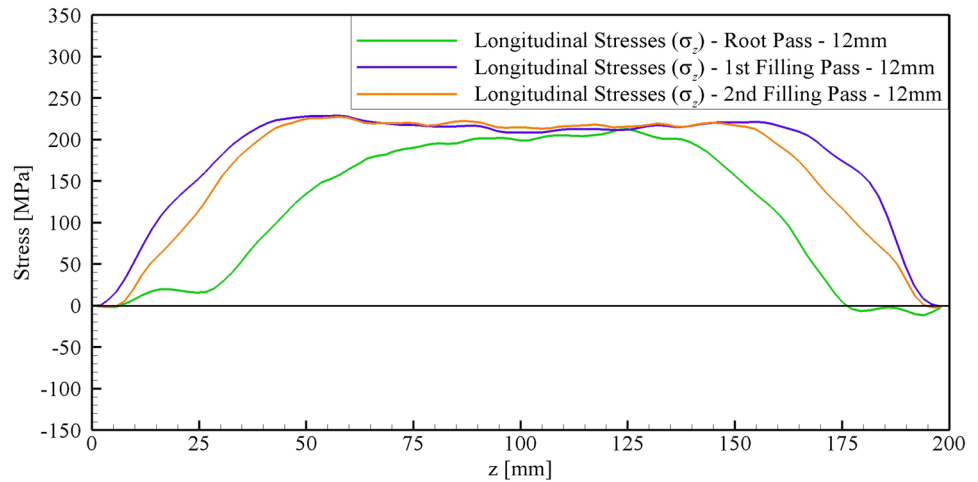
of transverse stresses is lower than the one of longitudinal ones (around half). It should be emphasized that the edge influences the transverse stresses, typically in cases in which welded plates are short, as reported by other authors such as Radaj [37].

Figure 22 shows the longitudinal stresses on the top of the plate along a transversal section at 65 mm from the beginning of the weld bead for each pass. Variations around the centerline of the weld bead (up to 7 mm) may have appeared due to the visco-plastic effects that occur at high temperatures which are not included in the numerical model. Typical behavior of longitudinal stresses is observed: tensile stresses near the weld bead and compression stresses far from it. Additionally, a larger zone with tensile stresses is noticed for the first and the second filling passes by comparison with the root pass.

6 Conclusions

The study reported in this paper used a methodology based on the finite element technique and the Gaussian heat

Fig. 20 Longitudinal stresses on the *top* of the plate along a *line* 12 mm from the weld bead and parallel to it

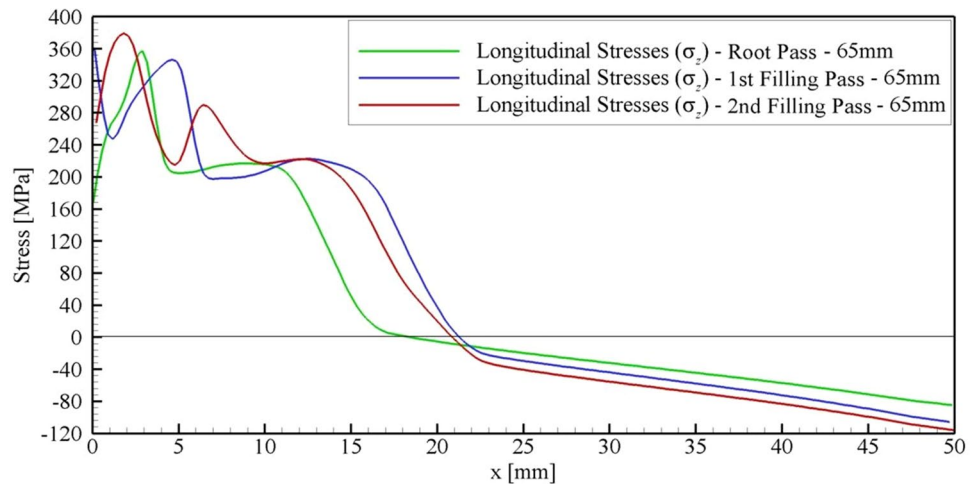**Fig. 21** Transverse stresses on the *top* of the plate along a *line* 12 mm from the weld bead and parallel to it

J Braz. Soc. Mech. Sci. Eng. (2017) 39:1245–1258

1257

Fig. 22 Longitudinal stresses at 65 mm from the beginning of the weld bead for each pass

source model to simulate a multi-pass single V-groove weld in butt joint of AISI 304L stainless steel, using the conventional MIG/MAG process. Numerical results of thermal and mechanical fields for the case study were compared with those obtained from the experiments developed at the laboratory of research in welding engineering (LAPES–FURG).

In the thermal analysis, the fusion zone shape obtained numerically agreed with the experimental one, with differences ranging from 2.0 to 12.2 % along the fusion zone boundary. The thermal cycles at different positions for the three passes were compared with experiments (by thermocouples) and good agreement was obtained regarding the peaks of the temperature and the cooling rates.

In the mechanical analysis, the deformed shape of plates was adequately simulated. The angular distortion obtained numerically agreed with the experimental one measured with 3D coordinate table. The residual stresses generated by the welding process were evaluated and had behaviors previously reported by other authors. After cooling, tensile stresses were observed in regions near the welding bead and compressive ones in regions far from there. The importance of using the element birth and death technique was observed, mainly in the mechanical analysis, since this technique avoids the influence of elements that belong to the welding material before the instant that is filled.

This paper showed that this methodology is a good proposal to model the MIG/MAG process for stainless steel. Besides, it is an excellent auxiliary tool to investigate and design welded structures. Nevertheless, several advances are still necessary because of the complexity of the phenomena, such as the inclusion of weaving, annealing effects and initial residual stresses in the methodology.

References

1. Friedman E (1975) Thermomechanical analysis of the welding process using the finite element method. J Press Vessel Technol 97:206–213
2. Lindgren LE (2001) Modelling for residual stresses and deformations due to welding-knowing what isn't necessary to know. Math Model Weld Phenom 6:491–518
3. Dong P (2003) The mechanics of residual stress distributions in girth welds. In: Procedures of the Second International Conference on Integrity of High Temperature Welds, London, p 185–196
4. Brickstad B, Josefson BL (1998) A parametric study of residual stresses in multi-pass butt-welded stainless steel pipes. Int J Press Vessels Pip 75:11–25
5. Capriccioli A, Frosi P (2009) Multipurpose ANSYS FE procedure for welding processes simulation. Fusion Eng Des 84:546–553
6. Coret M, Combescure A (2002) A mesomodel for the numerical simulation of the multiphasic behavior of materials under anisothermal loading (application to two low-carbon steels). Int J Mech Sci 44:1947–1963
7. Wu CS, Hu QX, Gao JQ (2009) An adaptive heat source model for finite-element analysis of key hole plasma arc welding. Comput Mater Sci 46:167–172
8. El-Ahmar W (2007) Robustesse de la simulation numérique du soudage TIG de structures 3D en acier 316L. Ph.D. thesis, Institut National des Sciences Appliquées de Lyon, Lyon
9. Rosenthal D (1941) Mathematical theory of heat distribution during welding and cutting. Weld J 20:220–234
10. Pavelic V et al (1969) Experimental and computed temperature histories in gas tungsten arc welding of thin plates. Weld J Res Suppl 48(7):295
11. Eagar TW, Tsai NS (1983) Temperature fields produced by traveling distributed heat sources. Weld J 62:346–355
12. Cho SH, Kim JW (2002) Analysis of residual stress in carbon steel weldment incorporating phase transformations. Sci Technol Weld Join 7:212–216
13. Deng D, Murakawa H, Liang W (2008) Numerical and experimental investigations on welding residual stress in multi-pass butt-welded austenitic stainless steel pipe. Comput Mater Sci 42:234–244
14. Rayamyaki P, Karkhin VA, Khomich PN (2007) Determination of the main characteristics of the temperature field for the

1258

J Braz. Soc. Mech. Sci. Eng. (2017) 39:1245–1258

evaluation of the type of solidification of weld metal in fusion welding. Weld Int 8:600–604

15. Balasubramanian KR, Siva Shanmugam N, Buvanashekaran G, Sankaranayanasamy K (2008) Numerical and experimental investigation of laser beam welding of AISI304 stainless steel sheet. Adv Prod Eng Manag 2:93–105

16. Zaeh MF, Schober A (2008) Approach for modelling process effects during friction stir welding of composite extruded profiles. Adv Mater Res 43:105–110

17. Ziolkowski M, Brauer H (2009) Modeling of Seebeck effect in eletron beam deeep welding of dissimilar metals. Int J Comput Math Electr Electron Eng 28:140–153

18. Goldak JA, Chakravarti A, Bibby M (1984) A new finite element model for welding heat sources. Metall Trans 15:299–305

19. Wahab MA, Painter MJ, Davies MH (1998) The prediction of the temperature distribution and weld pool geometry in the gas metal arc welding process. J Mater Process Technol 77:233–239

20. Wilkening WW, Snow JL (1993) Analysis of welding induced residual stresses with the ADINA-system. Comput Struct 47:767–786

21. Hong J, Tsai C, Dong P (1998) Assessment of numerical procedures for residual stress analysis of multipass welds. Weld J Am Weld Soc 77:372–382

22. Lee CH, Chang KH (2007) Three-dimensional finite element simulation of residual stresses in circumferential welds of steel pipe including pipe diameter effects. Mater Sci Eng A 487(1–2):210–218

23. Malik AM, Qureshia EM, Dar NU, Khan I (2008) Analysis of circumferentially arc welded thin-walled cylinders to investigate the residual stress fields. J Thin Walled Struct 46:1391–1401

24. Hu H, Argyropoulos SA (1996) Mathematical modeling of solidification and melting: a review. Modell Simul Mater Sci Eng 4:371–396

25. Sorensen MB (1999) Simulation of welding distortion in ship section. Ph.D. thesis, University of Denmark, Lyngby, Denmark

26. Teng TL, Fung CP, Chang PH, Yang WC (2001) Analysis of residual stresses and distortions in T-joint fillet welds. Int J Press Vessels Pip 78:523–538

27. Gery D, Long H, Maropoulos P (2005) Effects of welding speed, energy input and heat source distribution on temperature variations in butt joint welding. J Mater Process Technol 167:393–401

28. Smith M, Smith A (2009) Net bead-on-plate round robin: comparison of transient thermal predictions and measurements. Int J Press Vessels Pip 86:96–109

29. Paloposki T, Liedquist L (2005) Steel emissivity at high temperatures. VTT Tiedotteita, Research Notes 2299, Otamedia Oy, Espoo, Finland

30. Araújo DB (2012). Estudo de distorções em soldagem com uso de técnicas numéricas e de otimização. Doctoral dissertation, Universidade Federal de Uberlândia, Uberlândia (**in portuguese**)

31. Goldak JA, Akhlaghi M (2005) Computational welding mechanics. Springer, New York

32. Tamma KK, Namburu RR (1990) Recent advances, trends and new perspectives via enthalpy-based finite element formulations for applications to solidification problems. Int J Numer Meth Eng 30:803–820

33. Deng D, Murakawa H (2006) Numerical simulation of temperature field and residual stress in multi-pass welds in stainless steel pipe and comparison with experimental measurements. Comput Mater Sci 37:269–277

34. Touloukian YS, Dewitt DP (1970) Thermophysical properties of matter–the TPRC data series. Thermal radiative properties: metallic elements and alloys. Data Book, vol 7

35. Ohms C et al (2009) Net tg1: residual stress assessment by neutron diffraction and finite element modeling on a single bead weld on a steel plate. Int J Press Vessels Pip 86:63–72

36. Committee AIH (1990) Properties and selection–irons, steels, and high-performance alloys. ASM Int 1:140–194

37. Radaj D (2003) Welding residual stresses and distortion: calculation and measurement, Woodhead Publishing Limited, Cambridge